Energy Conversion and Management 173 (2018) 113–122

Contents lists available at ScienceDirect

Energy Conversion and Management

journal homepage: www.elsevier.com/locate/enconman

Hydrogen storage on $LaNi_{5-x}Sn_x$. Experimental and phenomenological Model-based analysis

D.G. Oliva[a], M. Fuentes[a], E.M. Borzone[b], G.O. Meyer[b,c], P.A. Aguirre[a,*]

[a] Instituto de Desarrollo y Diseño (INGAR), Consejo Nacional de Investigaciones Científicas y Técnicas (CONICET). Avellaneda 3657, S3002GJC Santa Fe, Argentina
[b] Comisión Nacional de Energía Atómica, Centro Atómico Bariloche, Av. Bustillo 9500, S.C. de Bariloche, Argentina
[c] Instituto Balseiro, Universidad Nacional de Cuyo, CONICET, Argentina

ARTICLE INFO

Keywords:
Hydrogen storage
Hydrogen solid storage
Hydride-forming metals
Mathematical model
Process modelling, simulation and optimization

ABSTRACT

Three hydride-forming metals ($LaNi_5$, $LaNi_{4.73}Sn_{0.27}$, and $LaNi_{4.55}Sn_{0.45}$) have been studied as solid phase hydrogen storage material in batch experiments using pure hydrogen and temperatures ranging from 300 K to 340 K. This process mainly involves: physisorption of hydrogen gas molecules; chemisorption and dissociation of hydrogen molecules; surface penetration of hydrogen atoms; hydride formation; and diffusion of hydrogen atoms through hydride-forming metal. In case the material is fully hydrided, hydride formation ceases and diffusion proceeds on the fully hydrided material.

A phenomenological model was developed by aggregating the first four mechanisms in a single sorption kinetic term involving a first-order driving force, the remaining mechanism being the atomic diffusion in the hydride-forming material. The driving force is computed between external partial pressure and equilibrium pressure according to the Pressure-Composition-Temperature model (PCT). The corresponding parameters for an empirical PCT were estimated from equilibrium data. This equation is more suitable for process engineering optimization due to the smoothness in its concentration domain. Specific sorption rate and diffusion coefficients of the process were also estimated from dynamic data. From a sensitivity analysis, productivity proved to be related to particle diameter. In the frame of batch processes, the global rate is dominated by the sorption kinetic term at the beginning of the experiments with the material being free from hydride, whereas with more than 5–10% of the material being hydrided, diffusion dominates the process. $LaNi_5$ shows higher hydrogen storage capacity than $LaNi_{4.73}Sn_{0.27}$ and $LaNi_{4.55}Sn_{0.45}$ within the investigated temperature and pressure ranges. Diffusion and sorption kinetic limited regions were identified from a sensitivity analysis of process productivity and normalized marginal values. The present work is oriented to modeling, designing, and optimizing storage and purification devices.

1. Introduction

Future energy networks based on hydrogen as a carrier have been proposed in several previous works [1–10]. The storage process is a key component in these networks. Depending on the final application, several technologies have been studied and compared in the literature [11–18]. More specifically, hydrogen storage in hydride-forming materials (HFM) has been extensively investigated. Storage and purification are important concerns in the development of this energy carrier [19–24]. $LaNi_{5-x}Sn_x$ alloys are good HFM candidates because of their low pressure and good global kinetic rates at room temperature. Furthermore, they present high cycling stability and good volumetric capacities [25–30].

Kinetics of these metal hydrides has been studied in order to map the reaction mechanisms of hydrogen charge and discharge and identify possible rate limiting steps [25]. A simplified model obtained by aggregating all mechanisms in only one kinetic expression was previously used by our work team [31,32]. It was embedded in an optimization model for hydrogen purification process design, including charge, venting, and discharge stages. Apparent activation energies are rarely reported; and there exist discrepancies as regards which steps are suggested for controlling the overall rate [33]. So, there is considerable interest in the literature about kinetics models for designers to optimize devices design and model their performance within some ranges of pressure and temperature for a specific application.

Hydrogen storage process mainly involves: physisorption of hydrogen gas molecules; chemisorption and dissociation of hydrogen molecules; surface penetration of hydrogen atoms; hydride formation

* Corresponding author.
E-mail address: paguir@santafe-conicet.gov.ar (P.A. Aguirre).

https://doi.org/10.1016/j.enconman.2018.07.041
Received 8 May 2018; Received in revised form 10 July 2018; Accepted 13 July 2018

Nomenclature

C	atomic H concentration [mol cm^{-3}]
D	diffusion coefficient [cm^2 s^{-1}]
H	Henry constant [mol cm^{-3} MPa^{-1}]
ΔH	enthalpy variation [J mol^{-1}]
P	pressure [MPa]
R	universal gas constant [J mol^{-1} K^{-1}]
T	temperature [K]
V	volume [cm^3]
a	parameter [cm^6 mol^{-2}]
b	parameter [mol cm^{-3}]
c	parameter [mol cm^{-3} K^{-1}]
d	parameter
k	specific sorption rate coefficient [mol MPa^{-1} cm^{-2} s^{-1}]
n	substance quantity [mol]
t	time [s]
v	sorption rate [mol s^{-1}]
gr	slope (parameter) of PCT curve

Subscripts

eq	equilibrium
exp	experimental
H_2	hydrogen
i	index
i_f	cardinality of i
in	initial
l	layer
m	medium, average
r	reactor

Greeks

α	equilibrium pressure factor
β	equilibrium pressure factor
γ	equilibrium pressure factor
δ	binary parameter
ε	binary parameter
ρ	binary parameter

and diffusion of hydrogen atoms through hydride-forming metal. In case the material is fully hydrided, hydride formation ceases and diffusion proceeds on the fully hydrided material [34].

In this work, a phenomenological model is proposed by aggregating the first four mechanisms above described in a single kinetic term involving first-order driving force, the remaining mechanism being atomic diffusion in the hydride-forming material. Thermodynamic equilibrium between gas phase and solid phase imposes a relationship between hydrogen potential in the gas phase and solid phase. The potential in the gas phase is assumed to be the partial pressure of hydrogen whereas the potential in solid phase is assumed proportional to the atomic hydrogen concentration in the solid phase. Equilibrium pressures as a function of atomic hydrogen concentration in the inner side of the gas/solid interphase correspond to the so called PCT diagram [26,35–37]. The driving force is computed between external partial pressure and equilibrium pressure according to the PCT model.

The qualitative behavior of PCT curves has been exhaustively described. Three main zones are distinguished. Initially, a low amount of hydrogen is dissolved in the metal structure for low pressure values. At higher pressure values, dissolved hydrogen evolves into a nucleation form. Then, the ordered phase is formed. In this region, the isotherm shows a plateau behavior; and its length indicates the amount of hydrogen that can be stored by means of an insignificant pressure change. This plateau pressure gains outstanding importance in engineering applications. For higher pressure values, only the ordered atomic phase is present in the metal hydride alloy. In this region, isotherm behavior changes; and incremental pressure leads to an insignificant increase of stored hydrogen. In previous works, [31,32], equilibrium pressure models representing partial profiles of PCT diagram were used. Some authors try to fit total curve by using several equations and thus they obtain a discontinuous function which cannot be used directly in optimization studies [38,39]. Here, HFM equilibrium pressure has been modeled using a single empirical function for a temperature range of 288 K to 388 K, achieving an overall representation of PCT curve that is suitable for optimization problems.

Parameter estimations of the PCT model were performed using both available data in the literature and our own experimental equilibrium values. Once PCT parameters were obtained, specific sorption rate and diffusion coefficients (k and D) are estimated using the proposed phenomenological model, PCT representation and our own experimental data. Dynamical experiments were carried out with pure hydrogen at temperature ranging from 300 K to 340 K and under different pressure values.

The paper is organized as follows: experimental setup is detailed in Section 2; the mathematical model is presented in Section 3; model results and limitations are discussed in Section 4; and finally, conclusions are drawn in Section 5.

2. Experimental setup

Three samples of $LaNi_{5-x}Sn_x$ alloys ($LaNi_5$, $LaNi_{4.73}Sn_{0.27}$ and $LaNi_{4.55}Sn_{0.45}$) were prepared. The alloys were prepared by arc melting under Ar, starting from the pure elements La (99.9%), Ni (99.95%), and Sn (99%). Alloys were remelted several times in order to improve their homogeneity. The resulting buttons, of about 10 g each, were then heat-treated at 1223 K for 48 h in individual quartz capsules containing Ar atmosphere. Chemical composition values were determined by atomic absorption spectroscopy. For details of the sample preparation procedure and alloys characteristics, see Ref. [33].

Sieverts-type volumetric equipment is used for these experiments. The reactor volume (about $7{\cdot}10^{-3}$ L) was previously calibrated. Fig. 1 represents the scheme used to measure hydrogen pressure into the

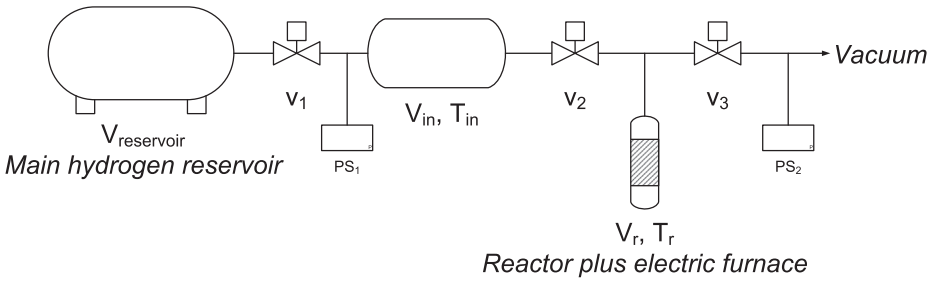

Fig. 1. Experimental setup of the hydrogen storage and discharge system.

reactor during storage on HFM. Process temperature around the reactor (measured by Pt-100 sensor) is set using an electric furnace (200 W Watlow) controlled by a 0.1 K step PID system. So, volume $V_{reservoir}$ has pure hydrogen; and volume V_r contains a previously activated, dehydrided alloy sample under vacuum conditions. At the beginning, valves v_1, v_2, and v_3 are closed (solenoid valves). Pressure in volume $V_{reservoir}$ is $P_{reservoir}$ while the compartments corresponding to volumes V_{in} and V_r are under vacuum. Next valve v_1 is opened; volume V_{in} is occupied by hydrogen; and pressure in $V_{reservoir}$ and V_{in} goes to P_{in}. After that, valve v_1 is closed and v_2 is opened. Here, sensor PS_1 (calibrated Baumer E914 transducer with pressure range from 0 to 1.6 MPa) starts to report experimental pressure data $P_{exp}(t)$; and the hydrogen charge experiment is started. Pressure does not differ in V_{in} or V_r during the experiment and varies over time. The experiment continues until the pressure reported by PS_1 reaches an invariable value. These data are used to perform the parameter estimation in the kinetic study (see Section 3.1). In order to clean the reactor and perform the next experience at a different initial pressure, valve v_2 is closed while v_3 is opened. Volume V_{in} maintains the same pressure while the vacuum pump discharges all the hydrogen stored in the metal alloy until sensor PS_2 reports pressure values close to vacuum condition. After that, valve v_3 is closed and v_2 is opened. Then, an experiment with a different initial pressure P_{in} is run; and the aforementioned steps are repeated. These cycles continue till pressure P_{in} reaches the lower bound planned in this study. This procedure is repeated for each $LaNi_{5-x}Sn_x$ alloy studied in this work and for different temperature settings at the furnace. For details on the sample preparation procedure and the resulting characteristics of the alloys, see Ref. [33].

3. Mathematical model

There exists a number of works devoted to specify the governing mechanisms of the hydrogen storage process [25,34,40,41]. As expressed, hydrogen storage process mainly involves: physisorption of hydrogen gas molecules; chemisorption and dissociation of hydrogen molecules; surface penetration of hydrogen atoms; hydride formation and diffusion of hydrogen atoms through hydride-forming metal. In case the material is fully hydrided, hydride formation ceases and diffusion proceeds on the fully hydrided material.

Following a schema used by many of these works [34], the results available in the literature indicate that the most common limiting mechanisms are atomic hydrogen diffusion inside the particle and hydrogen chemisorption [25]. In many cases, a combined schema is necessary [40,41].

The phenomenological model proposed in the present work aggregates the first four above mentioned mechanisms in a single kinetic term involving first-order driving force, the remaining mechanism being the atomic diffusion in the hydride-forming material. Driving force is computed between external partial pressure and equilibrium pressure according to the PCT model.

Other model assumptions are expressed as follows:

- Spherical particles of HFM with a single diameter are assumed.
- Only gas and solid phases are considered (i.e. the two phases inside HFM that were considered in previous works are neglected).

Equilibrium pressure is represented using an empirical model as follows:

$$P_{eq} = \alpha\beta\gamma \tag{1}$$

where

$$\alpha = 1-\exp(-aC_{eq}^2) \tag{2}$$

$$\beta = 0.1\exp\left[\frac{\Delta H}{RT_r}-\frac{\Delta S}{R} + gr\left(\frac{C_{eq}}{b-cT_r}-0.5\right)\right] \tag{3}$$

$$\gamma = \exp\left[d\left(1-\frac{C_{eq}}{b-cT_r}\right)^2\right] \tag{4}$$

and P_{eq} is equilibrium pressure of H_2 in gas phase; C_{eq} is atomic H equilibrium concentration at the metal surface; a, b, c, and d are parameters; ΔH and ΔS are the enthalpy and entropy of hydride formation respectively.

In Eq. (1), the first factor, α, describes the region where hydrogen in atomic form is dissolved in the metal alloy; the second factor, β, is related to the plateau behavior where hydrogen both dissolves in the metal alloy and coexists with the structured hydride; and the third factor, γ, represents the hydride saturation condition where atomic hydrogen is dissolved in the fully hydride metal.

The driving force governing the absorption depends on the difference between H_2 gas phase pressure and equilibrium pressure. The global sorption rate is calculated as follows:

$$v = k(P-P_{eq})4\pi r^2 \tag{5}$$

where k is specific sorption rate; r is particle radius; P is hydrogen gas pressure. Note that the specific sorption rate includes the four above mentioned mechanisms according to the suggestion made in previous works [34].

As stated before, H_2 concentration towards the outside of particle surface is determined by the hydrogen gas pressure, since diffusion in the gas phase is very fast. On the other hand, transport phenomena towards the inside of the particle play a significant role and need to be considered. HFM particle is geometrically assumed as a sphere. Radial discretization used in a previous work [42] is here adopted to model atomic H diffusion through the HFM-H solution. The sphere is divided into four equal volumes. The domain is presented in Fig. 2, where r_i and r_{mi} are regular and average radii of volume V_i, respectively.

$$r_{mi} = \left[\left(\frac{r_i^3}{2}\right) + \left(\frac{r_{i-1}^3}{2}\right)\right]^{1/3}, \quad i = 1, 2, 3, 4 \tag{6}$$

Discrete mass balance equation via diffusion mechanism is expressed as follows:

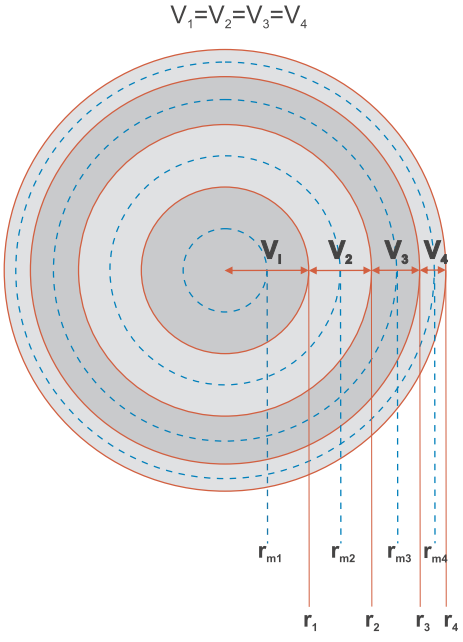

Fig. 2. HFM volume discretization scheme.

$$\frac{V_l(C_{i,t+1}-C_{i,t})}{\Delta t} = D\left[\delta\left(\frac{C_{i+1,t}-C_{i,t}}{r_{m_{i+1}}+r_{m_i}}4\pi r_i^2\right)-\varepsilon\left(\frac{C_{i,t}-C_{i-1,t}}{r_{m_i}+r_{m_{i-1}}}4\pi r_{i-1}^2\right) + \rho\left(\frac{C_{eq_t}-C_{i,t}}{r_i+r_{m_i}}4\pi r_i^2\right)\right];$$

$$\delta = \begin{cases}1, & if \quad 1 \le i < i_f\\ 0, & if \quad i = i_f\end{cases}; \quad \varepsilon\begin{cases}1, & if \quad 1 < i \le i_f\\ 0, & if \quad i = 1\end{cases}; \quad \rho\begin{cases}1, & if \quad i = i_f\\ 0, & if \quad 1 \le i < i_f\end{cases}$$

$$r_{i-1} = 0, \quad if \quad i = 1$$

$$Boundary \quad condition$$

$$D\left(\frac{C_{eq_t}-C_{i,t}}{r_i-r_{m_i}}4\pi r_i^2\right) = v, \quad if \quad i = i_f \tag{7}$$

where $C_{i,t}$ is the concentration of atomic H in the solid phase at any time t, v is the sorption rate, Δt is the time step, and D is the atomic H diffusion coefficient in the solid phase (HFM-H). Depending on δ, ε, and ρ (all binary) parameter values, Eq. (7) represents the global storage process in superficial, intermediate, and central HFM zones. Note that the value of layer volume V_l is the same for all defined V_i.

Gaseous H_2 molar quantity and vessel pressure are modeled as follows:

$$n_{H_2} = P_{in}\left(\frac{V_{in}+V_r}{RT}\right)-\frac{N_p}{2}\int_{V_{i=1}}^{V_{i=f}} C_i dV_i \tag{8}$$

$$P = \frac{n_{H_2}RT}{(V_{in}+V_r)} \tag{9}$$

where n_{H_2} is the amount of hydrogen moles in gas phase at any time; P_{in} is the initial pressure before starting the experiment; V_{in} and V_r are the volumes occupied by H_2 gas; T is system temperature; N_p is the number of HFM particles inside the vessel; dV is a differential volume; and P is vessel (H_2) pressure at any time.

3.1. Parameter estimation model via mathematical optimization

Parameter estimation is performed via optimization. The following nonlinear programming (NLP) problems are solved in order to find the minimum error between experimental values and predicted variables of the models. A first optimization is performed to estimate parameters of the PCT empirical model. These results are used in a second optimization to estimate phenomenological model parameters.

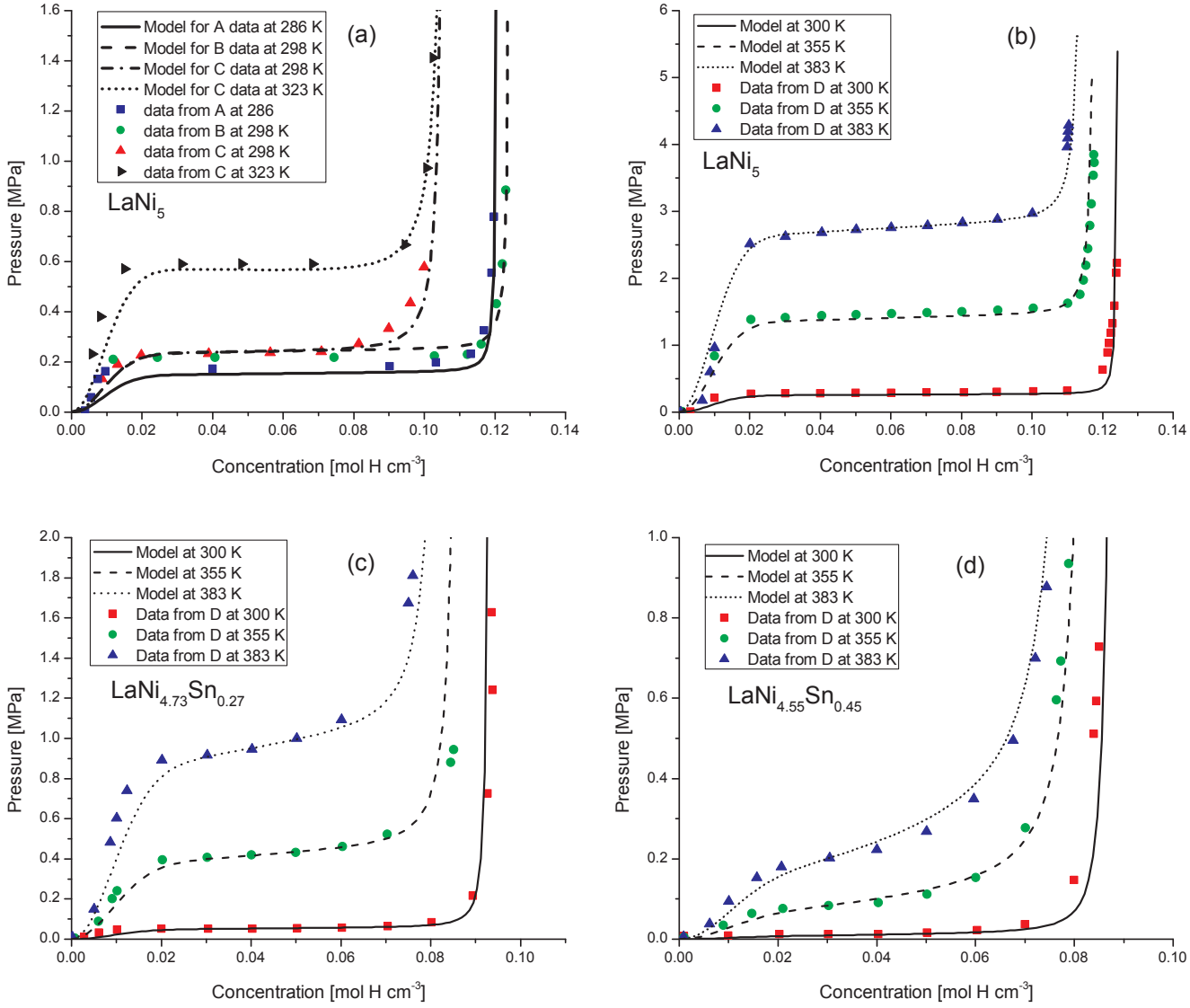

Fig. 3. Comparison between experimental data and PCT model predictions: (a) A, B, and C correspond to literature data ([45–47], respectively); and (b), (c), and (d) are our own data (D) for $LaNi_5$, $LaNi_{4.73}Sn_{0.27}$, and $LaNi_{4.55}Sn_{0.45}$, respectively [33].

$$\begin{array}{cc} \text{NLP1} & \text{NLP2} \\ \text{Min } error1 & \text{Min } error2 \\ \text{s. t.} & \text{s. t.} \\ \bar{f}(C_{eq}, P_{eq}, T_r) + \bar{g}(a, b, c, d, gr) = 0 & \bar{h}(t, C, P, P_{eq}) + \bar{m}(k, D) = 0 \\ error1 = \sum_{t=0}^{t=t_f} xp1(C_{eq}) & error2 = \sum_{t=0}^{t=t_f} xp2(t) \\ \left[\frac{P_{eq}(C_{eq}) - P_{exp}(C_{eq})}{P_{exp}(C_{eq})}\right]^2 = xp1(C_{eq}) & \left[\frac{P(t) - P_{exp}(t)}{P_{exp}(t)}\right]^2 = xp2(t) \\ xp1(C_{eq}) \geq 0 & xp2(t) \geq 0 \end{array} \quad (10)$$

where $error1$ is the absolute value of the relative error between experimental and predicted pressure values; $\bar{f}(C_{eq}, P_{eq}, T_r)$ and $\bar{g}(a, b, c, d, gr)$ are function vectors included in Eq. (1); $xp1(C_{eq})$ is an auxiliary variable computing the relative difference among predicted and experimental values. As a result, a, b, c, d and gr parameters are calculated for different HFM-type particles. In the second nonlinear programming, $\bar{h}(t, C, P, P_{eq})$ and $\bar{m}(k, D)$ are function vectors including Eqs. (1)–(9); $xp2(t)$ is an auxiliary variable computing the relative difference among predicted and experimental values. From the optimization problem solution, parameters k and D of the phenomenological model are calculated. In this work, NLPs were solved using CONOPT in GAMS environment [43,44].

4. Results and discussion

4.1. PCT model parameter estimation

Parameter estimation is intended to determine values for the unknown parameters with the aim of maximizing the probability that the model will predict the values obtained from the experiments. Experimental PCT equilibrium values for $LaNi_5$ are available in literature, and some profiles have been analyzed here. Fig. 3(a) shows the PCT model adjustment using A, B, and C experimental data extracted from the literature ([45–47], respectively). Estimated parameters values from NLP1 solution are summarized in Table1.

As observed, the proposed model adequately represents the total profile of PCT curve. To the best of our knowledge, there are no works including similar results. Previous proposals only achieve partial representations (plateau zone, mainly).

As a consequence of both data dispersion shown in Fig. 3(a) and the lack of information on the other investigated metals, the authors decided to use experimental data obtained by our task group (identified as D in Table 1) to adjust the PCT model [33]. Profiles for all metals at 300 K, 355 K, and 383 K are depicted in Fig. 3(b–d). PCT model parameter values have been included in Table 1.

4.2. Phenomenological model: Case study and parameter estimation results

Spheres of 10 μm-diameter are considered to represent the system performance for all investigated HFM. However, a sensitivity analysis of particle radii values is presented in Section 4.3. Experimental sequences are summarized in Table 2.

PCT model parameters to represent the equilibrium pressure of HFM particles have been obtained and are presented above.

Phenomenological model parameters k and D (used in Eqs. (5) and (7), respectively) are estimated from NLP2 solution. Optimal parameters are summarized in Table 3.

As observed in Table 3, specific sorption rate coefficient values (k) seem to have a similar magnitude order for all metals. However, $LaNi_{4.55}Sn_{0.45}$ presents the highest parameter value. It is well established that pressure dependence of gas phase reaction rates mainly arises from collisional energy transfer [48]. Determining the quantity of energy transferred per collision between reactant and bath-gas molecules is essential to perform any calculation of a sorption rate coefficient that is pressure-dependent. This is a complex task that has been subject of extensive experimental and theoretical investigation; empirical models can be used for that purpose [49]. The derivation of analytical expressions for $k(T, P)$ could become the object of future works.

Diffusion coefficient grows as Sn increases in HFM-type composition. Since Sn increases in metal composition, a faster absorption of hydrogen is achieved. Storage times for $LaNi_{4.73}Sn_{0.27}$ and $LaNi_{4.55}Sn_{0.45}$ are faster than $LaNi_5$ at the same initial pressure value. As expected, hydrogen storage capacity decreases as temperature rises, thus extending storage time. PCT equilibrium pressure curves (Fig. 3) also account for such behaviors. Note that, for high temperatures, the PCT profile denotes a decrease in the driving force (the pressure difference between a system and its equilibrium conditions). $LaNi_5$ shows higher hydrogen storage capacity than $LaNi_{4.73}Sn_{0.27}$, and $LaNi_{4.55}Sn_{0.45}$ in the investigated temperature and pressure ranges. These results are observed in previous works and are well represented by the proposed phenomenological model.

Fig. 4 shows a comparison among estimated and predicted values of system pressure for $LaNi_5$, $LaNi_{4.73}Sn_{0.27}$, and $LaNi_{4.55}Sn_{0.45}$ at 310 K. As observed, a suitable model adjustment is achieved for all HFM types. Fig. 5 depicts the percentage error for all experiments in Table 2 between experimental and model pressures. Then, the error is represented vs. pressure-time evolution. For lower times, maximum errors are observed in all HFM materials since high pressure variation in short times is observed at this zone. Mayor errors are found in $LaNi_{4.55}Sn_{0.55}$ (close to 6%) and this is because pressure decreases faster in this material. Nevertheless, percentage errors in the remaining zones are lower than 2%.

Table 1
PCT model parameters. $^*\Delta H$ and ΔS values are extracted by Ref. [33]

	Assumed			Estimated				
	T [K]	ΔH^* [J mol^{-1}]	ΔS^* [J mol^{-1} K^{-1}]	a [cm^3 mol H]	b [mol H cm^{-3}]	c [mol H cm^{-3} K^{-1}]	d	gr
$LaNi_5$ (A)	286	−27000	−98	6500	0.156	1.15e−4	0.001	0.13
$LaNi_5$ (B)	298				0.161			
$LaNi_5$ (C)	298				0.146		0.01	
$LaNi_5$ (C)	323				0.15			0
$LaNi_5$ (D)	300				0.161		0.001	0.13
	355							
	383							
$LaNi_{4.73}Sn_{0.27}$ (D)	300	−33000	−105		0.132		0.01	0.4
	355							
	383							
$LaNi_{4.55}Sn_{0.45}$ (D)	300	−35000	−100		0.114	5e−5	0.1	2
	355							
	383							

Table 2
Experimental sequences of initial pressure values analyzed for each HFM at different temperatures.

HFM	Mean reactor temperature (K)	HFM mass sample (g)	Initial pressure values (MPa)
$LaNi_5$	300	0.332	1.44, 1.26, 1.11, 0.96, 0.82, 0.70, 0.58 and 0.48
	310	0.314	1.30, 1.17, 1.05, 0.94, 0.85, 0.77 and 0.69
$LaNi_{4.73}Sn_{0.27}$	300	0.334	1.00, 0.86, 0.74, 0.63, 0.53, 0.43 and 0.35
	310	0.346	1.01, 0.90, 0.80, 0.71, 0.63, 0.56 and 0.50
	320	0.358	0.99, 0.86, 0.74, 0.63, 0.52 and 0.43
	340	0.341	1.00, 0.91, 0.84, 0.77, 0.72, 0.66, 0.62, 0.58, 0.55, 0.52 and 0.49
$LaNi_{4.55}Sn_{0.45}$	300	0.333	1.05, 0.93, 0.81, 0.70, 0.60, 0.51, 0.43, 0.35, 0.28, 0.22 and 0.16
	310	0.333	1.02, 0.93, 0.86, 0.79, 0.73, 0.67, 0.63, 0.58, 0.55 and 0.51
	320	0.330	1.00, 0.91, 0.84, 0.77, 0.70, 0.65, 0.60, 0.56, 0.53, 0.49, 0.46, 0.44, 0.42, 0.40, 0.38 and 0.36
	340	0.339	0.89, 0.78, 0.68, 0.58, 0.49, 0.41, 0.34, 0.27 and 0.21

Table 3
Results of parameter estimation for different HFM.

	k [mol H MPa^{-1} cm^{-2} s^{-1}]				D [cm^2 s^{-1}]
	300 K	310 K	320 K	340 K	
$LaNi_5$	1.36e−5	6.07e−4			1.6e−9
$LaNi_{4.73}Sn_{0.27}$	8.64e−6	9.32e−6	9.83e−6	1.01e−5	3.5e−9
$LaNi_{4.55}Sn_{0.45}$	3.03e−5	3.21e−5	3.43e−5	3.6e−5	9.7e−9

4.3. Sensitivity analysis

4.3.1. Particle diameter

For attaining the aforementioned results, a diameter of 10 μm is assumed. Here, a sensitivity analysis on the relationship between storage time and particle diameter is shown in Fig. 6. Experiments with different particle diameters were not developed in this work, so validation will be proposed in future communications. As observed in the literature, storage time decreases for small particles. In practice, a deterioration of HFM is observed during the cycling process. This phenomenon is observed in previous works that compare storage and discharge during cycle's evolution for $LaNi_5$ [50]. After a certain number of cycles, decrepitating effects appear; and then both the size of HFM particle and storage times decrease.

As depicted in Fig. 7, atomic hydrogen concentration varies along particle radius; and that variation is appreciable when particle diameter is increased. In all cases, mass transfer diffusive problems are significant.

4.3.2. Partial and fully hydrided final conditions

In order to show different hydrided final conditions, two simulations by varying HFM mass are performed. Fig. 8(a and b) shows the results obtained for 0.3 g and 3 g of 10 μm $LaNi_5$ particles, at 300 K and 0.8 MPa initial pressure, respectively.

In Fig. 8(a) the surface concentration reaches its final value almost instantaneously. At this point, surface is totally hydrided. This value remains constant till the storage process is finished. At the beginning, partial hydridation in the HFM particle bulk is observed. At steady state condition, all particles are fully hydrided. A different behavior is observed in Fig. 8(b). At the beginning of the process, surface concentration reaches its maximum value, i.e. surface is totally hydrided. Part of the bulk is also almost fully hydrided. Then, surface and surrounding concentrations decrease while core concentration values continue to increase up to the final value. This final concentration value is related to the plateau region of PCT curve (see Fig. 3(b)). At this concentration values, HFM particles are partially hydrided, i.e. particles have capacity enough to store more hydrogen. However, system and equilibrium pressures are the same; surface and bulk concentrations are equal and reached the steady state condition, i.e. diffusion or sorption no longer takes place.

4.3.3. Productivity. Reaction kinetic versus diffusion limitation

Metal hydriding through hydrogen gas storage can be carried forward departing from empty metal to full or partial hydriding metal. Also, it can be carried forward departing from partial hydriding metal to full or partial hydriding metal. Operational modes are defined according to the hydriding percentage interval (*HPI*). The hydriding percentage refers to the total hydrogen that can be stored depending on HFM capacity. Each mode has its productivity (*Pr*) and is defined as the amount of atomic hydrogen moles stored per grams of metal and per second (mol H gr^{-1} s^{-1}). *Pr* depends on both diffusion coefficient and specific storage coefficient.

Eq. (11) represents the NLP problem involving Eqs. (1)–(9) to maximize the *Pr* value for the given diffusion coefficient and specific storage rate values.

$$\begin{aligned} &\text{Max } Pr \\ &\text{s. t.} \\ &\bar{h}(t, C, P, P_{eq}) + \bar{m}(k, D) = 0 \end{aligned} \tag{11}$$

As an auxiliary result, normalized marginal productivities related with the specific sorption rate coefficient ($Pr_{m,k}$) and diffusion coefficient ($Pr_{m,D}$) are obtained. They are defined as follows:

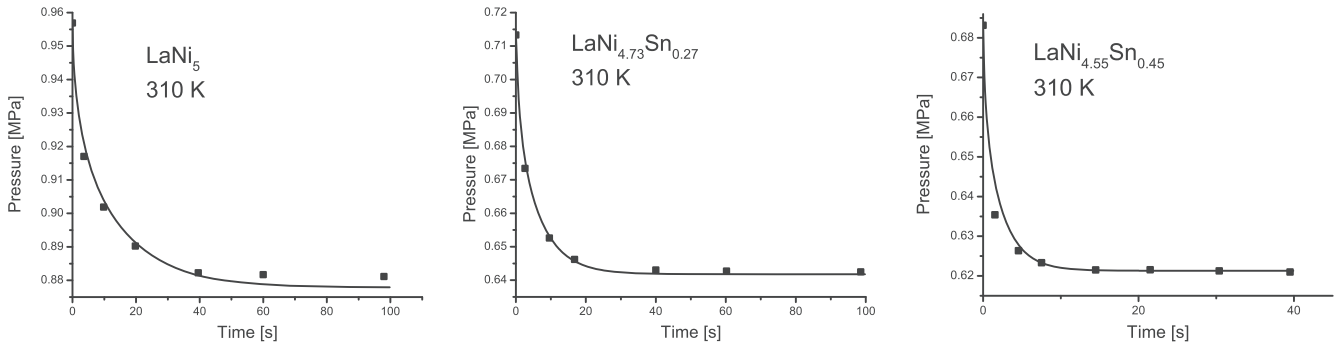

Fig. 4. Experimental and predicted values of pressure for HFM system.

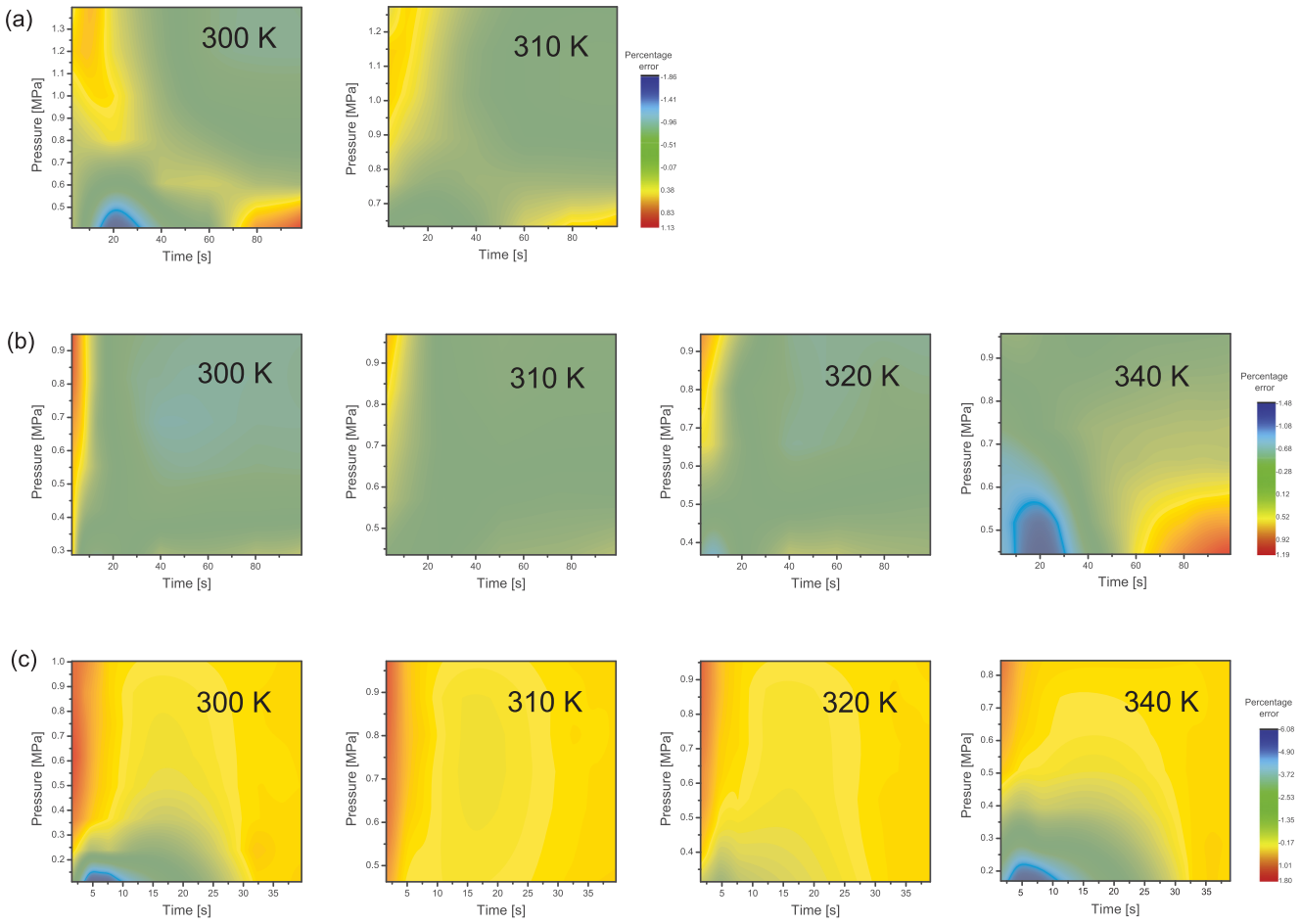

Fig. 5. Percentage errors between experimental and predicted pressure values vs pressure-time evolution. (a) LaNi5, (b) $LaNi_{4.73}Sn_{0.27}$ and (c) $LaNi_{4.55}Sn_{0.45}$.

$$Pr_{m,k} = \frac{\partial Pr}{\partial k}\left(\frac{k}{Pr}\right)$$

and

$$Pr_{m,D} = \frac{\partial Pr}{\partial D}\left(\frac{D}{Pr}\right)$$

Indeed, a normalized marginal productivities difference (Pr_{dif}) is defined as:

$$Pr_{dif} = Pr_{m,D} - Pr_{m,k}$$

Pr_{dif} values allow to identify when the process is diffusion or kinetic limited.

As an example, Fig. 9(a and b) shows productivity and normalized marginal difference values for $LaNi_5$, respectively (multiple simulations of Eq. (11) with different values of diffusion and specific sorption rate coefficients are performed to build Fig. 9). 10 μm-diameter particles and an operational temperature of 300 K are considered. Simulations from 0 to 10, 10 to 40, and 40 to 70 *HPIs* are performed (identified as Simulations I, II, and III, respectively). As observed in Fig. 9(a), productivity decreases 60% and 72% in Simulations II and III, respectively, when compared to Simulation I. In Fig. 9(b), the black line delimits diffusion and kinetic limited regions. Above this line, the process behaves as diffusion limited; and bellow, it behaves as kinetic limited. A black square point is sited in each simulation to show real conditions here experienced. As observed, a mixed control is obtained in Simulation I; and diffusion limited processes are distinguished in both Simulations II and III. Similar analyses were made for $LaNi_{4.73}Sn_{0.27}$, and $LaNi_{4.55}Sn_{0.45}$, and results (not shown) keep the same trends.

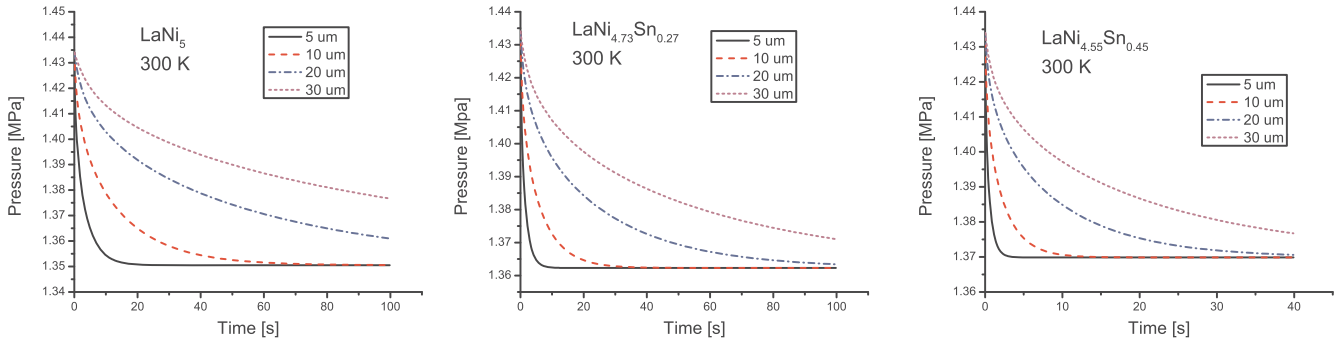

Fig. 6. Effects of particle diameter on storage time.

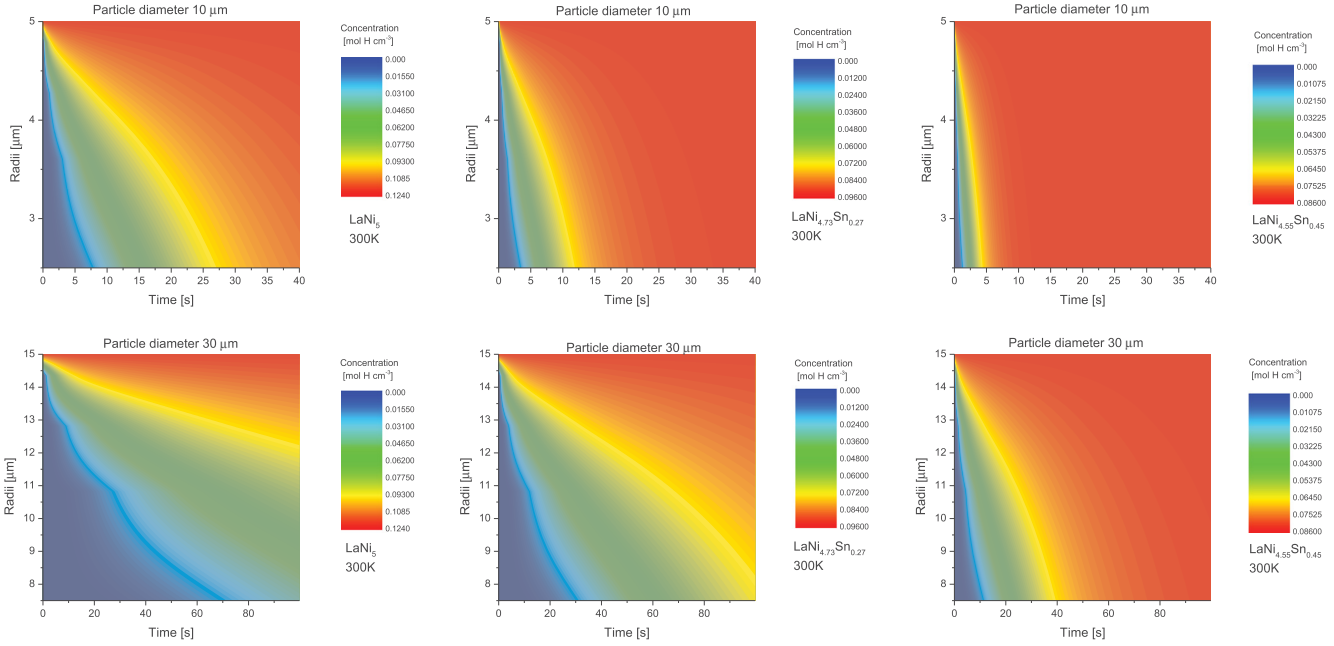

Fig. 7. Effects of particle diameter on atomic hydrogen concentration along particle radius.

5. Conclusions

In this work, an empirical model for Pressure-Composition-Temperature curves and a phenomenological model for H_2 absorption on hydride-forming materials are presented. Based on the results attained during this study, the following conclusions can be drawn:

– The empirical model allows representing the total profile of Pressure-Composition-Temperature curves used to calculate the driving force involved in the storage process. Previous advances only considered the plateau region of this curve. Parameters of Pressure-Composition-Temperature curve model for three hydride-forming materials were obtained.

– Specific sorption rate and diffusion coefficients were estimated. Sorption rate coefficient values seem to have a similar magnitude order for all metals. Correlation between Sn compositions in

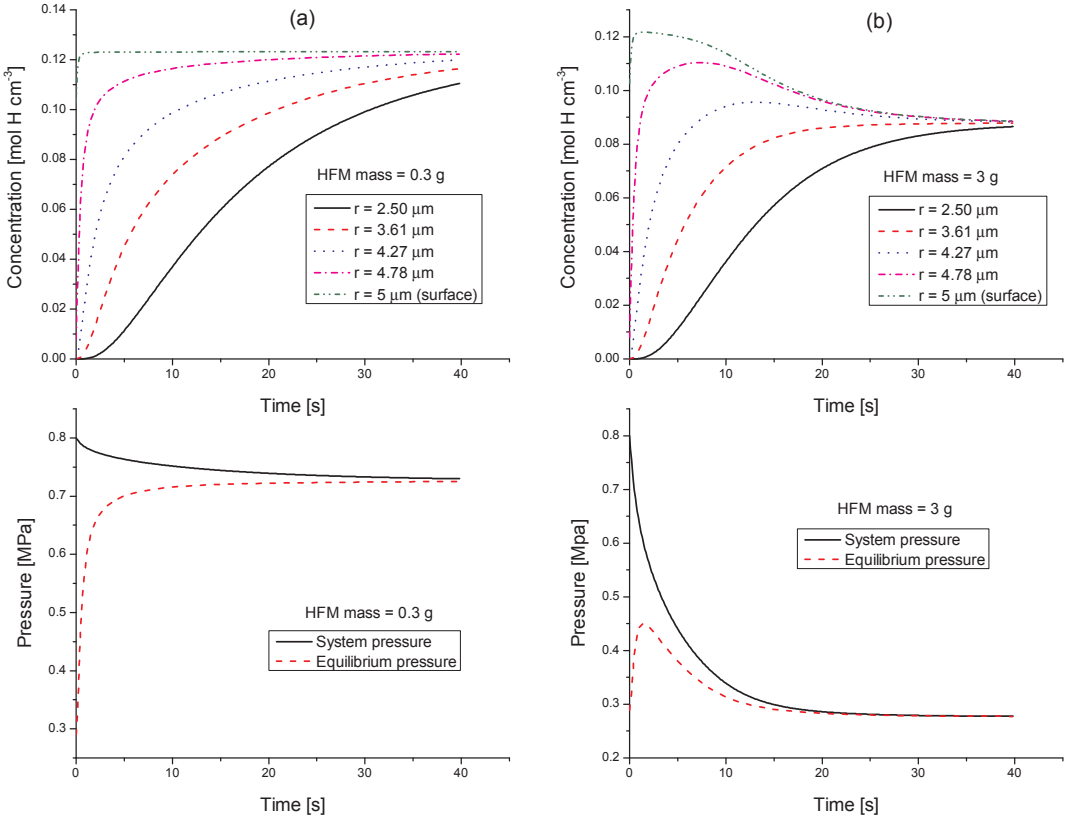

Fig. 8. Concentration and pressure profiles for: (a) 0.3 g, and (b) 3 g of 10 μm $LaNi_5$ particles at 300 K and 0.8 MPa initial pressure.

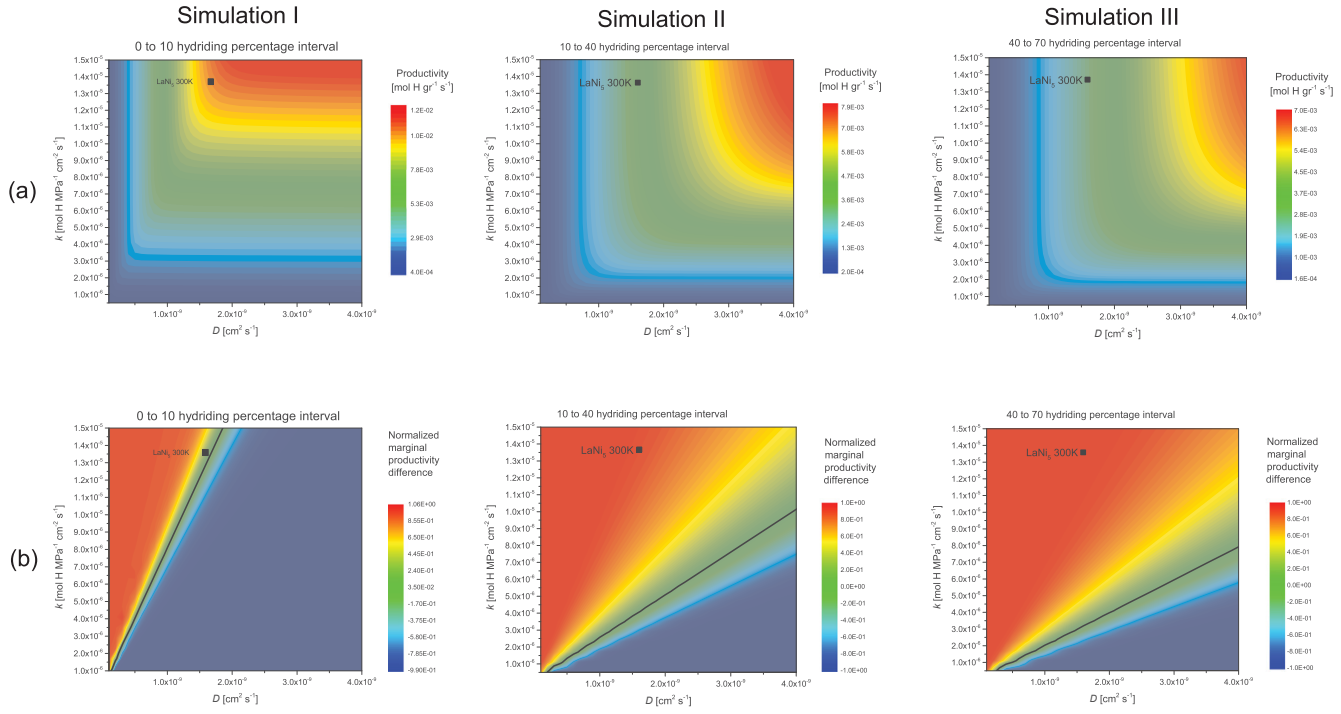

Fig. 9. Productivity as a function of diffusivity and sorption rate coefficients, sensitivity analysis using normalized marginal productivity difference values for 10 μm particles and operational temperature of 300 K.

hydride-forming materials and diffusion values are observed. Diffusion coefficient increases as Sn increases in the metal.

- The effect of particle diameter in hydride-forming materials on hydrogen storage capacity was evaluated. As expected, a significant mass transfer limitation was detected when the particle diameter increases for all investigated hydride-forming materials.
- $LaNi_5$ shows higher hydrogen storage capacity than $LaNi_{4.73}Sn_{0.27}$, and $LaNi_{4.55}Sn_{0.45}$ in the investigated temperature and pressure ranges. $LaNi_5$ storage process is slower than in the other alloys.
- Different concentration profiles related to full and partial hydridation final conditions were depicted and analyzed by varying mass value of hydride-forming materials.
- Diffusion and kinetic limited regions were identified from a sensitivity analysis of process productivity and normalized marginal difference values. In the presented example, $LaNi_5$ hydridation shows as a mixed limited process from 0 to 10 hydriding percentage interval, and then, diffusion phenomena manage the process.

The proposed model and estimated parameters are useful to evaluate trends in developing configurations for a new reactor using these hydride-forming materials and to perform process optimizations depending on technological purification requirements. Future works will be focused on using this approach to model the industrial implementation of a cycling process to obtain pure H_2 from furnaces' gas stream [51].

Acknowledgements

The authors acknowledge financial support provided by Consejo Nacional de Investigaciones Científicas y Técnicas (CONICET), Universidad Nacional del Litoral, Universidad Tecnológica Nacional and Agencia Nacional de Promoción Científica y Tecnológica (ANPCyT) of Argentina.

References

[1] Kim J, Lee Y, Moon I. Optimization of a hydrogen supply chain under demand uncertainty. Int J Hydrog Energy 2008;33:4715–29. https://doi.org/10.1016/j.ijhydene.2008.06.007.
[2] Almansoori A, Shah N. Design and operation of a future hydrogen supply chain: multi-period model. Int J Hydrog Energy 2009;34:7883–97. https://doi.org/10.1016/j.ijhydene.2009.07.109.
[3] Almansoori A, Shah N. Design and operation of a future hydrogen supply chain: snapshot model. Chem Eng Res Des 2006;84:423–38.
[4] Almansoori A, Shah N. Design and operation of a stochastic hydrogen supply chain network under demand uncertainty. Int J Hydrog Energy 2012;37:3965–77. https://doi.org/10.1016/j.ijhydene.2011.11.091.
[5] Almansoori A, Betancourt-Torcat A. Design of optimization model for a hydrogen supply chain under emission constraints – a case study of Germany. Energy 2016;111:414–29. https://doi.org/10.1016/j.energy.2016.05.123.
[6] Guillén-Gosálbez G, Mele FD, Grossmann IE. A bi-criterion optimization approach for the design and planning of hydrogen supply chains for vehicle use. AIChE J 2010;56:650–67.
[7] Maroufmashat A, Fowler M, Sattari Khavas S, Elkamel A, Roshandel R, Hajimiragha A. Mixed integer linear programing based approach for optimal planning and operation of a smart urban energy network to support the hydrogen economy. Int J Hydrog Energy 2016;41:7700–16. https://doi.org/10.1016/j.ijhydene.2015.08.038.
[8] Le Duigou A, Quéméré M-M, Marion P, Menanteau P, Decarre S, Sinegre L, et al. Hydrogen pathways in France: results of the HyFrance3 Project. Energy Policy 2013;62:1562–9. https://doi.org/10.1016/j.enpol.2013.06.094.
[9] Hwangbo S, Heo S, Yoo C. Network modeling of future hydrogen production by combining conventional steam methane reforming and a cascade of waste biogas treatment processes under uncertain demand conditions. Energy Convers Manag 2018;165:316–33. https://doi.org/10.1016/j.enconman.2018.03.069.
[10] Konstantinopoulos SA, Anastasiadis AG, Vokas GA, Kondylis GP, Polyzakis A. Optimal management of hydrogen storage in stochastic smart microgrid operation. Int J Hydrog Energy 2018;43:490–9. https://doi.org/10.1016/j.ijhydene.2017.06.116.
[11] Lim KL, Kazemian H, Yaakob Z, Daud WRW. Solid-state materials and methods for hydrogen storage: a critical review. Chem Eng Technol n.d.;33:213–26. 10.1002/ceat.200900376.
[12] Bowman RC, Fultz B. Metallic hydrides I: hydrogen storage and other gas-phase applications. MRS Bull 2002;27:688–93. https://doi.org/10.1557/mrs2002.223.
[13] Koh JT, Goudy AJ, Huang P, Zhou G. A comparison of the hydriding and dehydriding kinetics of LaNI5 hydride. J Common Met 1989;153:89–100. https://doi.org/10.1016/0022-5088(89)90536-5.
[14] Mellouli S, Dhaou H, Askri F, Jemni A, Ben Nasrallah S. Hydrogen storage in metal hydride tanks equipped with metal foam heat exchanger. Int J Hydrog Energy 2009;34:9393–401. https://doi.org/10.1016/j.ijhydene.2009.09.043.
[15] Di Profio P, Arca S, Rossi F, Filipponi M. Comparison of hydrogen hydrates with existing hydrogen storage technologies: energetic and economic evaluations. Int J Hydrog Energy 2009;34:9173–80. https://doi.org/10.1016/j.ijhydene.2009.09.056.
[16] Mori D, Hirose K. Recent challenges of hydrogen storage technologies for fuel cell

vehicles. Int J Hydrog Energy 2009;34:4569–74. https://doi.org/10.1016/j.ijhydene.2008.07.115.
[17] Stamatakis E, Zoulias E, Tzamalis G, Massina Z, Analytis V, Christodoulou C, et al. Metal hydride hydrogen compressors: Current developments & early markets. Renew Energy 2018;127:850–62. https://doi.org/10.1016/j.renene.2018.04.073.
[18] Vivas FJ, De las Heras A, Segura F, Andújar JM. A review of energy management strategies for renewable hybrid energy systems with hydrogen backup. Renew Sustain Energy Rev 2018;82:126–55. https://doi.org/10.1016/j.rser.2017.09.014.
[19] Abdalla AM, Hossain S, Nisfindy OB, Azad AT, Dawood M, Azad AK. Hydrogen production, storage, transportation and key challenges with applications: a review. Energy Convers Manag 2018;165:602–27. https://doi.org/10.1016/j.enconman.2018.03.088.
[20] Amirante R, Cassone E, Distaso E, Tamburrano P. Overview on recent developments in energy storage: mechanical, electrochemical and hydrogen technologies. Energy Convers Manag 2017;132:372–87. https://doi.org/10.1016/j.enconman.2016.11.046.
[21] Sakintuna B, Lamari-Darkrim F, Hirscher M. Metal hydride materials for solid hydrogen storage: a review. Int J Hydrog Energy 2007;32:1121–40. https://doi.org/10.1016/j.ijhydene.2006.11.022.
[22] Bao Z, Yang F, Wu Z, Nyallang Nyamsi S, Zhang Z. Optimal design of metal hydride reactors based on CFD–Taguchi combined method. Energy Convers Manag 2013;65:322–30. https://doi.org/10.1016/j.enconman.2012.07.027.
[23] Gonzatti F, Farret FA. Mathematical and experimental basis to model energy storage systems composed of electrolyzer, metal hydrides and fuel cells. Energy Convers Manag 2017;132:241–50. https://doi.org/10.1016/j.enconman.2016.11.035.
[24] Marty P, Fourmigue J-F, Rango PD, Fruchart D, Charbonnier J. Numerical simulation of heat and mass transfer during the absorption of hydrogen in a magnesium hydride. Energy Convers Manag 2006;47:3632–43. https://doi.org/10.1016/j.enconman.2006.03.014.
[25] Blanco MV, Borzone EM, Baruj A, Meyer GO. Hydrogen sorption kinetics of La–Ni–Sn storage alloys. Int J Hydrog Energy 2014;39:5858–67. https://doi.org/10.1016/j.ijhydene.2014.01.125.
[26] Gray EM, Blach TP, Buckley CE. Stability of the hydrogen absorption and desorption plateaux in LaNi5–H: Part 5: H capacity. J Alloys Compd 1999;293–295:57–61. https://doi.org/10.1016/S0925-8388(99)00301-1.
[27] Luo S, Clewley JD, Luo W, Flanagan TB, Wade LA. Thermodynamic studies of the $LaNi_{5-x}Sn_x$-H system from x = 0 to 0.5. J Alloys Compd 1995;231:467–72. https://doi.org/10.1016/0925-8388(95)01871-9.
[28] Andreasen A, Vegge T, Pedersen AS. Compensation effect in the hydrogenation/dehydrogenation kinetics of metal hydrides. J Phys Chem B 2005;109:3340–4. https://doi.org/10.1021/jp0458755.
[29] Borzone EM, Blanco MV, Meyer GO, Baruj A. Cycling performance and hydriding kinetics of LaNi5 and $LaNi_{4.73}Sn_{0.27}$ alloys in the presence of CO. Int J Hydrog Energy 2014;39:10517–24. https://doi.org/10.1016/j.ijhydene.2014.05.004.
[30] Pentimalli M, Padella F, La Barbera A, Pilloni L, Imperi E. A metal hydride–polymer composite for hydrogen storage applications. Energy Convers Manag 2009;50:3140–6. https://doi.org/10.1016/j.enconman.2009.08.021.
[31] Talagañis BA, Meyer GO, Aguirre PA. Modeling and simulation of absorption–desorption cyclic processes for hydrogen storage-compression using metal hydrides. Int J Hydrog Energy 2011;36:13621–31. https://doi.org/10.1016/j.ijhydene.2011.07.139.
[32] Talagañis BA, Meyer GO, Oliva DG, Fuentes M, Aguirre PA. Modeling and optimal design of cyclic processes for hydrogen purification using hydride-forming metals. Int J Hydrog Energy 2014;39:18997–9008. https://doi.org/10.1016/j.ijhydene.2014.09.045.
[33] Borzone EM, Baruj A, Blanco MV, Meyer GO. Dynamic measurements of hydrogen reaction with $LaNi_{5x}Sn_x$ alloys. Int J Hydrog Energy 2013;38:7335–43. https://doi.org/10.1016/j.ijhydene.2013.04.035.
[34] Martin M, Gommel C, Borkhart C, Fromm E. Absorption and desorption kinetics of hydrogen storage alloys. J Alloys Compd 1996;238:193–201. https://doi.org/10.1016/0925-8388(96)02217-7.
[35] Sandrock G. A panoramic overview of hydrogen storage alloys from a gas reaction point of view. J Alloys Compd 1999;293–295:877–88. https://doi.org/10.1016/S0925-8388(99)00384-9.
[36] Nobile A, Bach HT, Romero J, Basinger RW. A computer-controlled apparatus for performing pressure–composition–temperature measurements on metal hydrides with protium, deuterium, and tritium. Rev Sci Instrum 2001;72:1775–80. https://doi.org/10.1063/1.1347979.
[37] Cheng HH, Deng XX, Li SL, Chen W, Chen DM, Yang K. Design of PC based high pressure hydrogen absorption/desorption apparatus. Int J Hydrog Energy 2007;32:3046–53. https://doi.org/10.1016/j.ijhydene.2007.01.010.
[38] Fang S, Zhou Z, Zhang J, Yao M, Feng F, Northwood DO. The application of mathematical models to the calculation of selected hydrogen storage properties (formation enthalpy and hysteresis) of AB2-type alloys. Int J Hydrog Energy 2000;25:143–9. https://doi.org/10.1016/S0360-3199(99)00032-4.
[39] Payá J, Linder M, Laurien E, Corberán JM. Mathematical models for the P-C–T characterization of hydrogen absorbing alloys. J Alloys Compd 2009;484:190–5. https://doi.org/10.1016/j.jallcom.2009.05.069.
[40] An XH, Pan YB, Luo Q, Zhang X, Zhang JY, Li Q. Application of a new kinetic model for the hydriding kinetics of $LaNi_{5-x}Al_x$ ($0 \le x \le 1.0$) alloys. J Alloys Compd 2010;506:63–9. https://doi.org/10.1016/j.jallcom.2010.07.016.
[41] Schweppe F, Martin M, Fromm E. Model on hydride formation describing surface control, diffusion control and transition regions. J Alloys Compd 1997;261:254–8. https://doi.org/10.1016/S0925-8388(97)00192-8.
[42] Henquín ER, Aguirre PA. Phenomenological model-based analysis of lithium batteries: discharge, charge, relaxation times studies, and cycles analysis. AIChE J 2015;61:90–102. https://doi.org/10.1002/aic.14618.
[43] Drud A. CONOPT: a GRG code for large sparse dynamic nonlinear optimization problems. Math Program 1985;31:153–91.
[44] Brooke A, Kendrick DA, Meeraus A, Rosenthal RE. GAMS: a user's guide. Scientific Press; 1988.
[45] Murray JJ, Post ML, Taylor JB. The thermodynamics of the LaNi5-H2 system by differential heat flow calorimetry I: techniques; the α + β two-phase region. J Common Met 1981;80:201–9. https://doi.org/10.1016/0022-5088(81)90093-X.
[46] Boser O. Hydrogen sorption in LaNi5. J Common Met 1976;46:91–9. https://doi.org/10.1016/0022-5088(76)90182-X.
[47] Luo S, Clewley JD, Flanagan TB, Bowman Jr. RC, Wade LA. Further studies of the isotherms of $LaNi_{5-x}Sn_x$–H for x = 0–0.5. J Alloys Compd 1998;267:171–81. https://doi.org/10.1016/S0925-8388(97)00536-7.
[48] Gilbert RG, Smith SC. Theory of unimolecular and recombination reactions. Oxford; Boston: Brookline Village, Mass: Blackwell Science Inc; 1990.
[49] Karlicek RF, Lowe IJ. Hydrogen diffusion in β-LaNi5 hydride. J Common Met 1980;73:219–25. https://doi.org/10.1016/0022-5088(80)90306-9.
[50] Borzone EM, Blanco MV, Baruj A, Meyer GO. Stability of $LaNi_{5-x}Sn_x$ cycled in hydrogen. Int J Hydrog Energy 2014;39:8791–6. https://doi.org/10.1016/j.ijhydene.2013.12.031.
[51] Borzone EM, Baruj A, Meyer GO. Design and operation of a hydrogen purification prototype based on metallic hydrides. J Alloys Compd 2017;695:2190–8. https://doi.org/10.1016/j.jallcom.2016.11.067.